HIGH FIDELITY SIMULATIONS FOR THE PREDICTION OF CAVITATION EROSION

Matevž Dular*

Laboratory for Water and Turbine Machines, University of Ljubljana, Slovenia

Jian Wang

Research Center of Fluid Machinery Engineering and Technology, Jiangsu University, China

Martin Petkovšek

Laboratory for Water and Turbine Machines, University of Ljubljana, Slovenia

ABSTRACT

We are comparing results of numerical simulations against high speed simultaneous observations of cavitation and cavitation erosion. We performed fully compressible, cavitating flow simulations to resolve the formation of the shock waves at cloud collapse – these are believed to be directly related to the formation of the damage. Good agreements were noticed between calculations and tests. Two high pressure peaks were found during one cavitation cycle. One relates to the cavitation collapse and the other one corresponds to the cavitation shed off, both contributing to a distinctive stepwise erosion damage growth pattern. Additional, more precise, simulations with much shorter time step were performed to investigate the processes of cavitation collapse and shedding off in more detail. There the importance of small cavitation structures which collapse independently of the main cloud was found. The present work shows a great potential for future development of techniques for accurate predictions of cavitation erosion by numerical means only.

KEYWORDS

Cavitation, Erosion, Computational Fluid Dynamics

1. INTRODUCTION

Since Rayleigh reported on the cavitation erosion issue on ship propellers in 1917, considerable progress has been made to discover its hydrodynamic mechanisms [1-4]. Two main mechanisms are usually discussed: the micro-jet and pressure shock wave. For the case of the micro-jet it is believed that the liquid jet penetrates the bubble as the surrounding pressure is imbalanced. The jet velocity can reach a magnitude order of 100 m/s, and when it impacts the solid wall enormous stresses that cause pit formation occur [5]. On the other hand the pressure shock wave approach, considers the bubbles to remain spherical during the collapse what, at the final stage causes a shock wave generation with a magnitude order of several MPa [6]. Fortes-Patella et al. [7] studied the interaction between shock wave emitted by the implosions of a spherical bubble and material deformation. They concluded that the cavitation induced damage is directly related to the pressure shock wave and the characteristics of material. Subsequently, they proposed a so-called energy cascade theory. It

* *Corresponding author:* Laboratory for Water and Turbine Machines, University of Ljubljana, Slovenia
phone: +386 4771 314, email: matevz.dular@fs.uni-lj.si

postulated that potential energy contained in a macro cavitation cloud, considering the conservation of energy, would transfer into the radiation of acoustic pressure wave, which might be emitted either by spherical bubble or vortex collapse as well as micro jet.
The rapidly development of computational power and numerical simulation technology, increase the potential and the accuracy of the methods for the prediction of cavitating flow and cavitation erosion power. Dular & Coutier-Delgosha [8] presented a prediction method of cavitation damage based on the micro-jet theory, by coupling a computational fluid dynamics (CFD) and the proposed erosion model.
In the present paper we are comparing results of numerical simulations against experimental data obtained by Petkovsek & Dular [9]. We performed fully compressible, cavitating flow simulations to resolve the formation of the shock waves at cloud collapse – these are believed to be directly related to the formation of the damage. We have shown that two pressure peaks occur during one cavitation cycle, what consequently explains why the damage observed during the experiments occurs also at times other than at cavitation cloud collapse. Also the importance of small cavitation structures which collapse independently of the main cloud was confirmed.

2. EXPERIMENT

The experiments were carried out in a cavitation loop test rig in the Laboratory for Water and Turbine Machines, University of Ljubljana. These are only briefly described here – for a more thorough description the reader should refer to [9].
A Venturi section, which has a converging angle of 18° and diverging angle of 8° was used. The size of the throat of the test section was $10\times10\text{mm}^2$. The geometry is shown in Fig. 1.

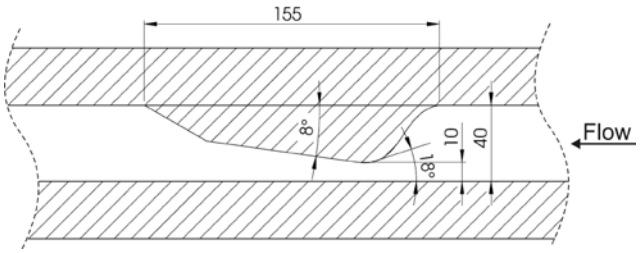

Fig. 1: The Venturi geometry.

The idea of the experiment was to simultaneously record images of cavitation structures and cavitation erosion. The upper side of the foil is covered by vapour structures that obstruct the view, hence one needs to look at the foil from the bottom side to see the damage. Consequently the whole test section had to be made of transparent material and equally important the foil had to be thin enough so that the cavitation damage which occurs on the side exposed to cavitation was also visible on the other side. Furthermore the damage needs to occur very rapidly so that one is able to record it by high speed cameras - we have chosen 10 μm thick aluminum foil and attached it to a Venturi section by a transparent two sided adhesive tape with thickness of 50 μm. Using this approach a sufficient pitting can be obtained in a few seconds.
The flow direction in Fig. 2 is from right to left. Cavitation cloud shedding begins with the cloud separation from the attached cavity. It then travels with the flow and collapses in a higher pressure region downstream. At the rear part of the attached cavity a back flow (re-entrant jet) forms that eventually cuts the cavity in two and causes a new separation of the cloud.

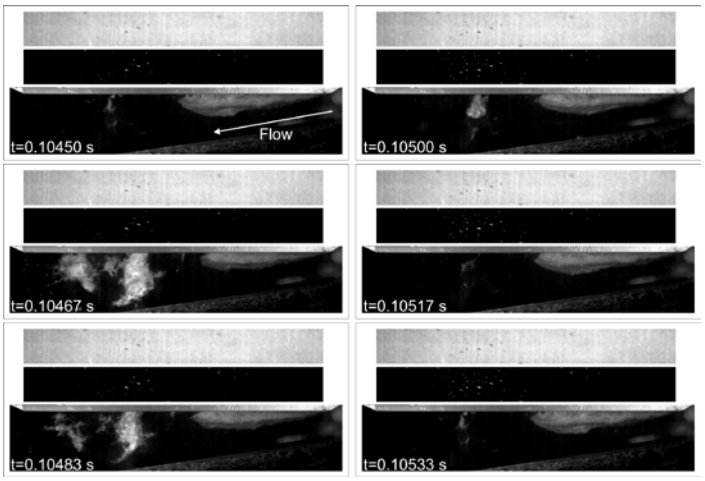

Fig. 2: Instantaneous image of the aluminum foil (top images), measured damage of the foil up to this instant (middle images) and instantaneous image of cavitation (bottom images) [9]. The flow is from the right to the left.

We can see that pits form immediately after the collapse of the cavitation cloud (in the present sequence we have two clouds that collapse at t=0.10500 s and 0.10517 s, respectively). It can also be seen that the region where most of the pitting occurs corresponds to the position of the cloud collapse. It is interesting to see that not a single pit forms but rather a cluster of them. We hypothesize that the shock wave from the cavitation cloud collapse interacted with several bubbles which were present in the vicinity of the wall (aluminum foil).

3. MATHEMATICAL MODELS

3.1 The governing equations and homogenous flow model

The applied governing equations were based on the conservation form of the Reynolds averaged Navier-Stokes equations, including mass continuity (1), momentum equation (2) and energy equation (3):

$$\frac{\partial \rho_m}{\partial t} + \frac{\partial}{\partial x_i}(\rho_m \overline{u_i}) = 0 \tag{1}$$

$$\frac{\partial(\rho_m \overline{u_i})}{\partial t} + \frac{\partial(\rho_m \overline{u_i u_j})}{\partial x_i} = -\frac{\partial p}{\partial x_i} + \frac{\partial}{\partial x_j}\left[\left(\mu_m + \mu_t\right)\left(\frac{\partial \overline{u_i}}{\partial x_j} + \frac{\partial \overline{u_j}}{\partial x_i} - \frac{2}{3}\delta_{ij}\frac{\partial \overline{u_k}}{\partial x_k}\right)\right] \tag{2}$$

$$\frac{\partial(\rho_m E)}{\partial t} + \nabla \cdot [\bar{u}(\rho_m E + p)] = \nabla \cdot (k_{eff} \nabla T) \tag{3}$$

where p is the pressure, ρ is the density, u is the velocity, μ and μ_t stand for the laminar viscosity and turbulent viscosity, δ_{ij} is the Kronecker delta function, $E = h - p/\rho_m + u^2/2$, h is the entropy, k_{eff} is the effective conductivity, α is the volume fraction. The subscripts m,l,v indicate the mixture, liquid and vapor, respectively.

The liquid phase and vapor phase are treated as a homogeneous mixture based on the volume of fraction. The mixture density and viscosity are defined as a function of vapor volume fraction.

3.2 Turbulence model

As known, the turbulence model plays a significant role in the prediction of cavitating flow. A modified Re-normalized group (RNG) k-ε model, proposed by Coutier-Delgosha et al. [10],

was employed in this work. It can successfully reduce the eddy viscosity by defining the turbulent viscosity as:

$$\mu_t = f(\rho_m) C_\mu \frac{k^2}{\varepsilon} \tag{4}$$

$$f(\rho_m) = \rho_v + \frac{(\rho_m - \rho_v)^n}{(\rho_l - \rho_v)^{n-1}} \tag{5}$$

where the coefficient C_μ=0.09, identical with k-ε model, and the exponent n=10.

3.3 Cavitation model

The vapor generation and disappearance are controlled by a mass transport equation model based on the vapor volume fraction, expressed as:

$$\frac{\partial \alpha_v}{\partial t} + \frac{\partial (\alpha_v u_j)}{\partial x_j} = \dot{m}^+ + \dot{m}^- \tag{6}$$

The source term $\dot{m}^+$ and $\dot{m}^-$ represent the mass rates of liquid evaporation and vapor condensation. In this paper, the Zwart-Gerber-Belamri model [11], deduced from the Rayleigh-Plesset equation, was applied, since it has, based on our previous experience, a precise cavitating prediction performance and a good convergence behavior. It is defined as:

$$\dot{m}^+ = F_{vap} \frac{3 r_{nuc} (1-\alpha_v) \rho_v}{R_B} \sqrt{\frac{2}{3} \frac{p_v - p}{\rho_l}}, \text{ if } p<p_v \tag{7}$$

$$\dot{m}^- = F_{cond} \frac{3 \alpha_v \rho_v}{R_B} \sqrt{\frac{2}{3} \frac{p - p_v}{\rho_l}}, \text{if } p>p_v \tag{8}$$

where F_{vap} and F_{cond} are the empirical calibration coefficients of evaporation and condensation, respectively, r_{nuc} stands for the nucleation site volume fraction, R_B is the nucleation site radius. Vaporization is initiated at nucleation sites, which can be regarded as the non-condensible gases. p_v represents the water vaporization pressure. The recommended values of these coefficients are: F_{vap}=50, F_{cond}=0.01, r_{nuc}=5×10^{-4}, R_B=2×10^{-6} m and p_v=3574Pa. As compressible approach was adopted the vapour obeyed the ideal gas law and the liquid density variation was described via Tait equation:

$$\rho_l = \rho_{ref} \sqrt[n]{\frac{p + B}{p_{ref} + B}} \tag{11}$$

where ρ_{ref} and p_{ref} denote the reference liquid density and pressure 200mm upstream of the Venturi section. As for constant B and n, they are 300MPa and 7 for water, respectively.

4. MODELING

To get a better accuracy and convergence behaviour, the structured hexahedral grid was generated to model the fluid computational domain. The refinement was made near the Venturi surface. The grid independence test was conducted on the basis of three kinds of mesh density. Considering the calculation time and accuracy, the medium grid size was

applied further on. The total number of the elements is about 0.5 million. The Y+ on the Venturi surface along with the chord length was in the order of 20.

4.1 Simulation setup

The commercial CFD code "ANSYS-Fluent" was used to solve the URANS equations summarized above. A mass flow rate and static pressure boundary conditions are imposed on the inlet and outlet respectively, strictly following the experimental data. Meanwhile, the turbulent intensity at the inlet is set as 3%. A no-slip wall is applied on the Venturi surface with standard wall function. The convergence criteria are all set to 10^{-4}. On the premise of ensuring the temporal accuracy, all the simulations were initiated by running the calculation under upwind scheme based on COUPLED algorithm for four shedding periods until a time-periodic solution has been reached, with a time step of 1.6×10^{-4} s. Afterwards, the algorithm was changed to the second-order scheme and the time step was reduced to 1.6×10^{-7} s to obtain a more precise resolution concerning to the cavity shedding off and collapse.

5. RESULTS

The cavity cloud shedding at σ=1.48 is first analyzed. The comparisons between computational results and experiments are made to validate the numerical simulations, as shown in Fig. 3. For the computational results, an isosurface of 10% vapor volume fractions are adopted. A good agreement can be noted between simulation and experiment results. We can see that the attached cavity sheds off at around t=t0+20Δt both in simulation and in experiment. Subsequently, the cloud cavity collapse occurs approximately at t=t0+45Δt. The inception of cavitation at the leading edge of the Venturi surface occurs earlier in the experiment - nevertheless we believe that the numerical simulation is still reliable for the investigation of the potential energy during the cavitation collapse, since the collapse time matches well between the experiment and the simulation.

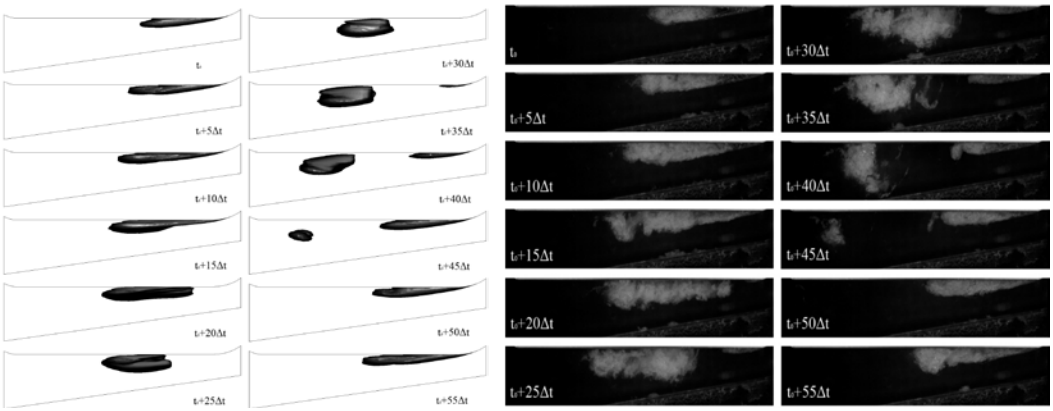

Fig. 3: Simulated (left) and observed (right) cavitation structure evolution, the flow direction is from right to left. σ=1.48 and v=24.7m/s.

For quantitative study of the relationship between the cavity evolution and the induced damage, the absolute pressure obtained from four monitor points on the Venturi surface are plotted together with the number of pits and integral damage area from the experiment [9], as a function of time. Point A is located near the throat of the Venturi (5 mm downstream), monitor D is located near the region where the bubble cloud collapse takes place (65 mm downstream of the Ventuiri thorat). Monitors B and C are placed between A and D (22 mm and 48 mm downstream of the Venturi throat, respectively).

The diagram in Fig. 4 shows the absolute pressure obtained at four monitor points and the number of pits and integral damage area from the experiment [9]. The simulation data

adopted here are obtained with a time step of 1.6×10^{-4} s. The exact cavity collapse times from the experiment are presented as vertical dash-dot lines in this diagram.

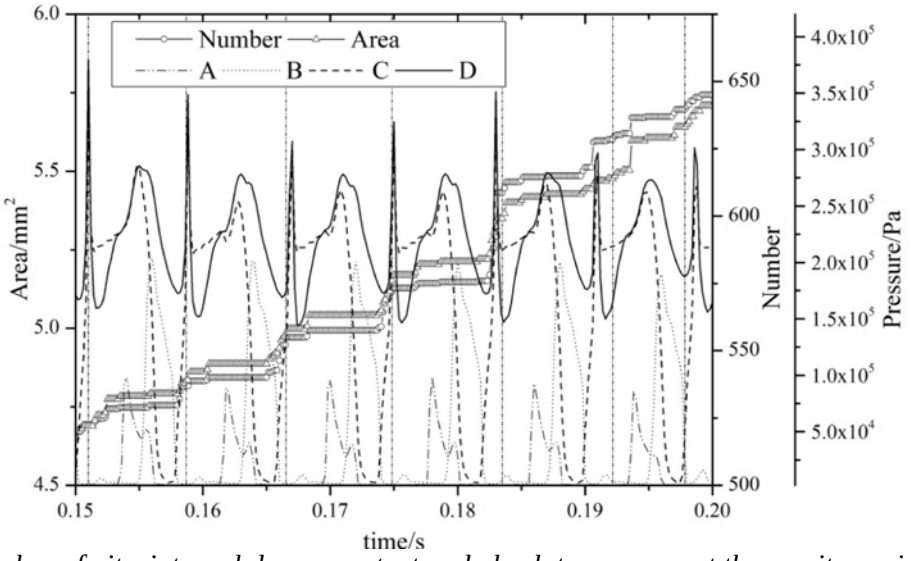

Fig. 4: Number of pits, integral damage extent and absolute pressure at the monitor points A, B, C, and D as a function of time. At cavitation number σ=1.48 and velocity at the Venturi throat v=24.7m/s, Reynolds number Re=247000.

It can be seen that with the time progressing, the number of the pits and the damaged area are not increasing at a constant pace. A considerable damage occurs only during a period of cloud collapse. More precisely, it can be noticed that some the damage is also generated just before the main cavitation cloud disappears.

As for the simulation, we can observe that there are two high pressure peaks in one cycle, especially at points C and D. The higher peak corresponds to the cloud collapse, while the other one is related to the moment of cavity shedding off. It can be seen that the pressures recorded at monitor D are the highest and reach up to 3.5×10^5 Pa. Considerable pressure increase from the cloud collapse is also seen by monitor C, while monitors A and B, which are further away from the collapse region, notice only a small disturbance in the pressure.

More precise simulations with a smaller time step 1.6×10^{-7} s were conducted to investigate the correlation between damage appearance, the cavitation cloud collapse and the shedding of the cloud. There are several pressure fluctuations before it reaches the highest point, which implies that the cavity collapse is not instantaneous. To understand the details of the collapse evolution, six instants are chosen to present the absolute pressure on the Venturi surface together with the cavitation, Fig. 5. The white dot in the graph represents the monitor D.

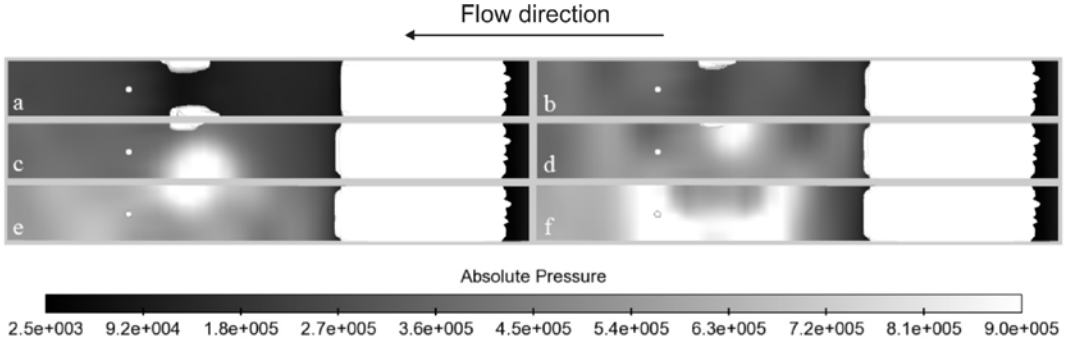

Fig. 5: Absolute pressure at the Venturi surface at times a to f during cavitation cloud collapse. σ=1.48 and v=24.7m/s. The flow direction is from right to left.

In the image a, there are two big bubbles clouds close to the side wall of the Venturi section and the pressure is low at this moment. The instant of the image b is chosen just after one of the bubble clouds below disappear. One can see that the shock wave has not arrived at the Venturi surface yet - this is why the pressure on the surface is still low. Several micro seconds later, the collapse shock wave impacts the surface (image c), where we can see a concentrated region of a very high pressure. Image d, illustrates that during the collapse of the other bubble cloud, some tiny bubbles around it also generate pressure shock waves as they collapse. In images e and f, one can see how the shock wave propagated through the region and after it is emitted at the origin of cloud collapse.

Similarly, Fig. 6 presents the evolutions of pressure and cavitation during the shedding process. The grey dot in the images represents the monitor A.

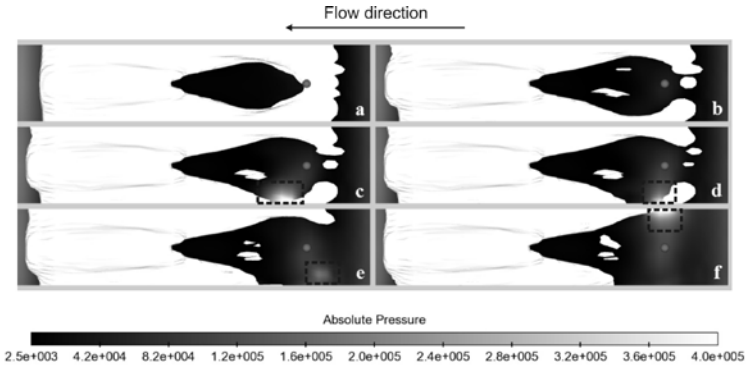

Fig. 6: Absolute pressure on Venturi surface at times a to f during cavitation shedding process. σ=1.48 and v=24.7m/s. The flow direction is from right to left.

In image a, we can see that the cavitation is beginning to shed, but no high pressure region can be seen yet. A pressure peak first appears after the cavitation breaks off (image c) – in a very small region (noted by a dashed square). After breaking off, a small bubble remains at the leading edge (image d). At time f, the cavitation begins to shed off on the other side of the channel, but there is no break off, so only one high pressure peak appears at this moment. This shows how and when the pressure peak is created during the shedding process, which eventually leads to a, previously hard to explain, damage near the throat of the Venturi.

6. CONCLUSION

In this paper, a compressible approach to simulate cavitating flow in a Venturi section was performed with two different time steps. The results were firstly validated against visualization experiments, and then some new insights into the formation of damage were drawn from the results. The conclusions can be given in several points:

- From the erosion tests, we see that most of the damages occurs at the point of cavitation cloud collapse. Yet it was also reported [9] that some damage occurs just before and after the cavitation cloud collapse, and even during the shedding process. The simulation results, obtained with a larger time step of 1.6×10^{-4} s, are in a good agreement with the visualization experiments. Absolute pressure on the Venturi surface as a function of time at four monitor points were compared with the erosion measurements. We observed two pressure peaks in one cycle. The higher one relates to the cloud collapse and the other corresponds to the shedding off the cloud from the attached part of the cavity, what partially explained a not rigorously stepwise trend of the damage occurrence.

- Instantaneous images of the absolute pressure on the Venturi surface, measured erosion damage of the foil and the instantaneous image of cavitation were analyzed simultaneously. It was found that the main damage occur at the cavitation cloud collapse, as a clear result of a very high pressure wave which is emitted at that instant. Besides this we were able to conclude that a somewhat less pronounced pressure peak occurs during the cloud shedding process – and that this also contributes to some cavitation erosion pits. There are also some indications that an almost negligible number of pits is generated during the growth of the attached cavitation.
- Finally, based on a more time resolved simulation (time step length was only 1.6×10^{-7} s), we observed instabilities during the collapse and the shedding of cavitation cloud. We were able to show that the cavitation collapse is not instantaneous and coherent – many tiny bubbles collapse prior and after the main clouds collapse and these also considerably contribute to the erosive energy potential of cavitating flow.

7. REFERENCES

[1] Kato, H., Konno, A., Maeda, M., and Yamaguchi, H.: Possibility of Quantitative Prediction of Cavitation Erosion without Model Test. *ASME J. Fluids Eng.*, 118(3), 1996, pp. 582–588.

[2] Berchiche, N., Franc, J. P., and Michel, J. M.: A Cavitation Erosion Model for Ductile Materials. *ASME J. Fluids Eng.*, 124(3), 2002, pp.601–606.

[3] Franc, J. P., Karimi, A., Chahine, G. L., and Riondet, M.: Impact Load Measurements in an Erosive Cavitating Flow. *ASME J. Fluids Eng.*, 133(12), 2011, pp.121301.

[4] Franc, J. P: Incubation Time and Cavitation Erosion Rate of Work-Hardening Materials. *ASME J. Fluids Eng.*, 131(2), 2009, pp. 021303.

[5] Franc, J. P., Riondet, M., Karimi, A., and Chahine, G. L.: Material and Velocity Effects on Cavitation Erosion Pitting. *Wear*, 274, 2012, pp.248-259.

[6] Wang, Y. C., and Brennen, C. E.: Shock Wave Development in the Collapse of A Cloud of Bubbles. *ASME. American Society of Mechanical Engineers*, 194, 1994 pp.15-19.

[7] Fortes-Patella, R., Archer, A., and Flageul C.: Numerical and Experimental Investigations on Cavitation Erosion. *IOP Conference Series: Earth and Environmental Science*, 15(2), 2012, pp. 022013.

[8] Dular, M., and Coutier-Delgosha, O.: Numerical Modelling of Cavitation Erosion," *Int. J. Numer. Meth. Fluids*, 61(12), 2009, pp. 1388–1410.

[9] Petkovšek, M., and Dular, M.: Simultaneous Observation of Cavitation Structures and Cavitation Erosion. *Wear*, 300(1), 2013, pp.55-64.

[10] Coutier-Delgosha, O., Fortes-Patella, R., and Reboud, J. L.: Evaluation of the Turbulence Model Influence on the Numerical Simulations of Unsteady Cavitation. *ASME J. Fluids Eng*., 125(1), 2003, pp. 38 - 45.

[11] Zwart, P., Gerber, A. G., and Belamri, T.: A Two-Phase Model for Predicting Cavitation Dynamics. *Proceedings of ICMF2004 International Conference on Multiphase Flow*, 2004 Yokohama, Japan.